Hindawi
Advances in Civil Engineering
Volume 2020, Article ID 8887040, 19 pages
https://doi.org/10.1155/2020/8887040

Research Article

Study of Deformation Behaviors and Mechanical Properties of Central Diaphragm in a Large-Span Loess Tunnel by the Upper Bench CD Method

Yanbin Luo, Zhou Shi, Jianxun Chen, Weiwei Liu, Yao Li, Yunfei Wu, and Haoyang Zhu

School of Highway, Chang'an University, Shaanxi, Xi'an 710064, China

Correspondence should be addressed to Zhou Shi; 519479162@qq.com and Weiwei Liu; liuwwchd@163.com

Received 4 March 2020; Revised 21 June 2020; Accepted 29 June 2020; Published 21 July 2020

Academic Editor: Hui Yao

The central diaphragm is often used to reduce the span to maintain the stability and safety of structure in the construction of large-span loess tunnel due to the structure complexities. In this paper, relying on the field monitoring and measurement for Wangcun tunnel in Huangling-Yan'an expressway expansion project, the crown settlement and horizontal convergence of primary support steel rib and central diaphragm steel rib during the construction are analyzed by the upper bench CD method. According to the internal force transfer, deformation coordination, and arch foot displacement between the two structures, the support system is regarded as the arch-beam fixed structure with three times of statically indeterminate and movable abutment under the loads, and the mechanical calculation model of sidewall steel rib and the central diaphragm structure bearing loads and deformation together is established. Finally, through the mechanical model mentioned above, the deformation characteristics of central diaphragm structure and the horizontal convergence in the upper bench of tunnel are calculated and analyzed. The research shows the following: (1) the accumulated settlement of sidewall steel rib in Part I is greater than that of the sidewall steel rib in Part II, and the accumulated settlement of each part at the support structure during the tunnel excavation is less than the reserved deformation of 150 mm specified in the tunnel excavation; (2) the settlement located at the waist and maximum excavation line position of central diaphragm is mainly affected by the excavation of Parts I and II in upper bench; (3) during the whole excavation process, the excavation of Part I and Part II has the greatest influence on the convergence at arch waist and the maximum excavation line position in Part I, and the convergence at the above two positions all experienced four stages of "convergence-expansion-convergence-gradual stability"; and (4) the errors between the horizontal convergence and the deformation of central diaphragm obtained by the mechanical model and the field monitoring data are between 12.7% and 27.5%. The calculated results are in good agreement with the actual situation. The research can provide a theoretical basis for the study of deformation and mechanical properties for support structure in the construction of large-span loess tunnel by the upper bench CD method.

1. Introduction

Along with the implementation of China's "The Belt and the Road" strategic plan and the rapid development of national economy and traffic construction in the western region, the number of motor vehicles has been increasing and the traffic volume has been increasingly saturated in recent years. Traffic congestion problems have seriously restricted the development of road traffic [1–6]. As the tunnel project is an irreversible project and the traffic route is nonrenewable resources, there are more and more single hole three-lane loess highway tunnels in new construction and reconstruction projects in the western region [7, 8]. Engineering practice showed that the soil disturbance area is large, the bearing arch is difficult to form, and there are no obvious signs before the soil collapse during the construction of large-span loess tunnel. In the shallow tunnel area, the surface cracks produce easily, and the surface settlement is difficult to be controlled during the tunnel construction, which increase the construction difficulties of large-span loess tunnel. A large number of single two-lane highway loess tunnels have been constructed in China during the past years, and there have appeared serious problems such as surface cracking, arch

settlement, lining deformation, and even collapse. Scholars have obtained some scientific research results and effectively guided the construction of project after many years of scientific research and engineering practice for loess tunnel [9–15]. For example, Chen et al. revealed the action mechanism that the system bolt could not restrain the deformation of loess tunnel, established the mechanical analysis method for the composite structure of steel rib and foot reinforcement bolt (pipe) (FRB) in loess tunnel, and proposed the rigid support theory that the steel rib is the main structure to control the deformation in loess tunnel [16]. At present, many scholars all over the world have made a lot of researches on the construction technology for single hole two-lane loess tunnel, but few of them have studied the deformation law and the mechanical characteristics of support structure for single hole three-lane long-span loess tunnel.

At present, the main construction methods for large-span loess tunnel are the bench method [17, 18], the central diaphragm method (CD) [19], the cross diaphragm method (CRD) [20–22], and the two-side pilot hole method [23, 24]. However, the engineering practice of large-span loess tunnel shows that the above four construction methods cannot meet the requirements of deformation control and construction efficiency at the same time. Therefore, based on the traditional CD method, the upper bench CD method came into being. The new construction method can not only effectively control the deformation of the tunnel, but also speed up the construction progress, improving the construction efficiency greatly [25]. The central diaphragm structure is often used as temporary support to maintain the stability of tunnel during the construction by upper bench CD method. The field monitoring and measurement results show that the central diaphragm structure often produces large deformation and complex stress characteristics in the process of tunnel excavation and support structure installation, which will induce a series of engineering problems and pose a great threat to the stability of tunnel structure and the safety of construction. The overall stability of support structure is closely related to the stress state of central diaphragm, and the stress safety of central diaphragm is of great significance to the safety and stability of the whole support structure. Therefore, with the application of upper bench CD method in engineering practice, the stability and stress state of central diaphragm structure have attracted the attention of academia.

Many scholars have studied the deformation and mechanical response of support structure in the construction of loess tunnel [13, 26–28]. The safety and stability of central diaphragm structure has also attracted the attention of many scholars, which is often used to reduce the excavation span and improve the structural stability for the structure safety of large-span loess tunnel. Zhang et al. analyzed the central diaphragm deformation in the CRD construction section for Xiamen East Passage by convergence metrology method. They proposed that the deformation of horizontal convergence was mainly caused by the deformation of central diaphragm [29]. Zhang studied the influence of construction in each excavation part on the primary support safety and the characteristics of stress and deformation during the construction of large section of soft stratum in the land section of Xiamen Xiang'an undersea tunnel buried by CRD method [30]. The results showed that the joint of upper part at the central diaphragm and the primary support vault was the weakest part for support structure during the construction by CRD method. Luo and Chen measured the horizontal convergence of tunnel first leading hole and the crown subsidence during the CRD construction by using the side measurement method through the total station [31]. Through the analysis of displacement time curve, the deformation law of central diaphragm was obtained. Zhang et al. analyzed the deformation characteristics of central diaphragm by establishing a mechanical model, while the sidewall steel rib and the central diaphragm are regarded as the arch structure and the beam structure whose two ends are fixed in the stratum, respectively, without considering the moment transfer and deformation coordination between the above two structures [32]. Based on the soil highway tunnel, Luo et al. studied the mechanical characteristics of central diaphragm structure for the large-span shallow soft surrounding rock tunnel constructed by CRD method and proposed the mechanical calculation model of central diaphragm structure. The steel rib of central diaphragm is regarded as the three times statically indeterminate beam structure with two ends fixed into soil under the action of horizontal load, without considering the displacement of both ends at the steel rib, the mechanical characteristics and deformation law for central diaphragm in different construction stages are obtained [33].

Generally speaking, the previous studies on the mechanical properties of central diaphragm mainly focused on the project construction by CD, CRD, and two-side pilot hole method, while the researches on the central diaphragm structure for large-span loess tunnel constructed by the upper bench CD method have not been studied. In addition, the numerical simulation and field monitoring are the main approaches used in the previous study. In terms of mechanical calculation model, the mechanical model for central diaphragm structure is too simplified and rough, the deformation coordination between the sidewall steel rib and the central diaphragm steel rib as well as the displacement at the arch foot of steel rib is not considered, and the stress of structural joint and the central diaphragm is not clear, which cannot truly reflect the bearing mode and mechanism of support structure in the construction process. Therefore, for the large-span loess tunnel constructed by upper bench CD method, the mechanical and deformation characteristics of central diaphragm structure need to be further studied, and the safety and stability of structure directly affect the construction safety and cause a series of engineering problems.

Based on the field monitoring of Wangcun tunnel project in Huangyan expressway, this paper analyzes and discusses the crown settlement and horizontal convergence of steel rib at sidewall and the central diaphragm structure during the construction by upper bench CD method and establishes the mechanical calculation model with the sidewall steel rib and the central diaphragm structure bearing loads and deformation together. According to the internal force transfer, deformation coordination, and arch

foot displacement between the two structures, the support system is regarded as the arch-beam fixed structure with three times of statically indeterminate and movable abutment under the loads. Through the mechanical model mentioned above, the deformation characteristics of central diaphragm structure and the horizontal convergence in the upper bench of tunnel are calculated and compared with the field monitoring data. The good agreement between the two results proves that the mechanical model and the calculation method have strong applicability and high reliability for the tunnel project. The study can provide theoretical basis for the analysis of mechanical and deformation characteristics for support structure during the construction of large-span loess tunnel by the upper bench CD method.

2. Engineering Overview

Huangling-Yan'an expressway expansion project is an important part of Xi'an-Yan'an expressway project. There are 36 tunnels (single tunnel) in the whole route, with a total length of 50.306 km, including 44.927 km/27 long tunnels, 4.254 km/6 medium tunnels, and 1.125 km/3 short tunnels. The tunnels satisfy the double hole six-lane design standard, with design speed of 100 km/h, maximum excavation span of 17.85 m, height of 12.18 m, flat rate of 0.67, and excavation area of 177.1 m^2, which are the highway loess tunnels with the largest excavation span around the world, and the first large-scale tunnel project crossing the loess stratum with high water content at present.

Wangcun tunnel is the key project of Huangling-Yan'an expressway expansion project. It is a curve separated double hole six-lane loess highway tunnel with a design speed of 100 km/h. The starting and ending pile number of tunnel left line is ZK11 + 560~ZK12 + 560, with a total length of 1000 m. The starting and ending pile number of tunnel right line is YK11 + 510~YK12 + 645, with a total length of 1135 m. The clear distance between the left and right lines is about 149 m, and the maximum buried depth of left and right lines is 93 m. The tunnel construction clearance is 14.5 m in clear width and 5.0 m in clear height; the maximum excavation span is 17.85 m and the maximum excavation height is 12.18 m, which belongs to the large-span loess tunnel. The upper bench CD method was adopted in the tunnel construction. The excavation diagram of this method is shown in Figure 1, and the detailed construction stage information is summarized in Table 1.

The landform of tunnel site is loess tableland, and the stratum of tunnel crossing is mainly quaternary lower Pleistocene Wucheng formation loess (Q1col), part of which is central Pleistocene Lishi formation loess (Q2col) and upper Pleistocene Malan formation loess (Q3col). The rock mass type of tunnel is Class V with single type. The groundwater in the tunnel site is not rich in general, and there is an aquifer in the Quaternary loess. The water content of rock mass is between 19.8% and 24.25%. The rock mass stability is poor, and there will be water dripping or seepage during excavation. The geological conditions of Wangcun tunnel are illustrated in Figure 2.

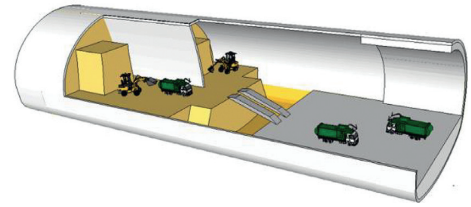

Figure 1: Schematic diagram of the upper bench CD method.

3. Observation Performance of Central Diaphragm Structure

3.1. Measuring Point Arrangement and Observation Frequency. Based on Wangcun tunnel, the crown settlement and horizontal convergence of support structure during the construction used upper bench CD method in tunnel section with Class V-level surrounding rock are monitored and measured on-site.

3.1.1. Crown Settlement of Support Structure. The total station reflective films are installed in Part I [including the vault (*A*), left arch waist (*B*), central diaphragm waist (*C*), and maximum excavation line position (*D* and *E*)], and Part II [including the vault (*F*), right arch waist (*G*), and maximum excavation line position at right arch (*H*)], and the change of tunnel clearance convergence during the excavation process is observed by TOPCON OS-602G total station. The measuring points are arranged as shown in Figure 3.

3.1.2. Horizontal Convergence of Support Structure. According to the field construction situation, the total station reflective films are set at the arch waist (*BC*) and the maximum excavation line position (*DE*) in Part I, and the change of tunnel horizontal convergence during the excavation process is observed by TOPCON OS-602G total station. The reflective film and field measurement situation are illustrated in Figures 4 and 5.

The observation frequency in this tunnel satisfied the requirements of technology code for highway tunnel, as shown in Table 2.

3.2. Deformation Analysis for Support Structure. Table 3 shows the accumulated crown settlement value at the monitoring sections in Wangcun tunnel. According to the field monitoring data and the specific situation of support structure during the construction, the deformation laws of each monitoring section are basically the same. In this paper, only YK11 + 931 section and YK11 + 928 are selected for analysis. The crown settlement and horizontal convergence of these two sections are shown in Figures 6–9, respectively.

According to Table 3, the cumulative settlement value of sidewall steel rib (*A*, *B*, and *D*) in Part I is between 34 and 131 mm, with an average of 67.6 mm; the cumulative settlement value of sidewall steel rib (*F*, *G*, and *H*) in Part II is between 16 and 65 mm, with an average of 29.3 mm. In the process of tunnel excavation, the settlement time curves of

Table 1: Construction stage of the upper bench CD method.

Excavation stage	Construction activity	Diagram
I	Excavate Part I, install the sidewall steel rib and central diaphragm steel rib, and construct the foot reinforcement bolt	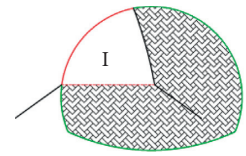
II	Excavate Part II, install the sidewall steel rib, and construct the foot reinforcement bolt	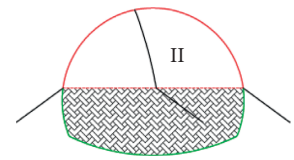
III	Excavate Part III and install the sidewall steel rib	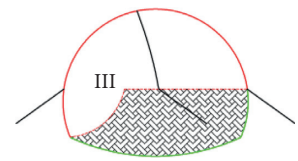
IV	Excavate Part IV and install the sidewall steel rib	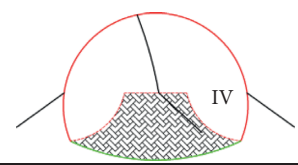
V	Dismantle the central diaphragm steel rib, excavate the core soil of bottom, and install the temporary invert	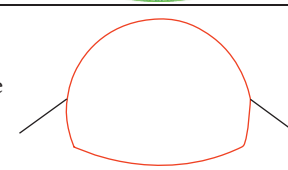

Figure 2: The geological conditions of Wangcun tunnel.

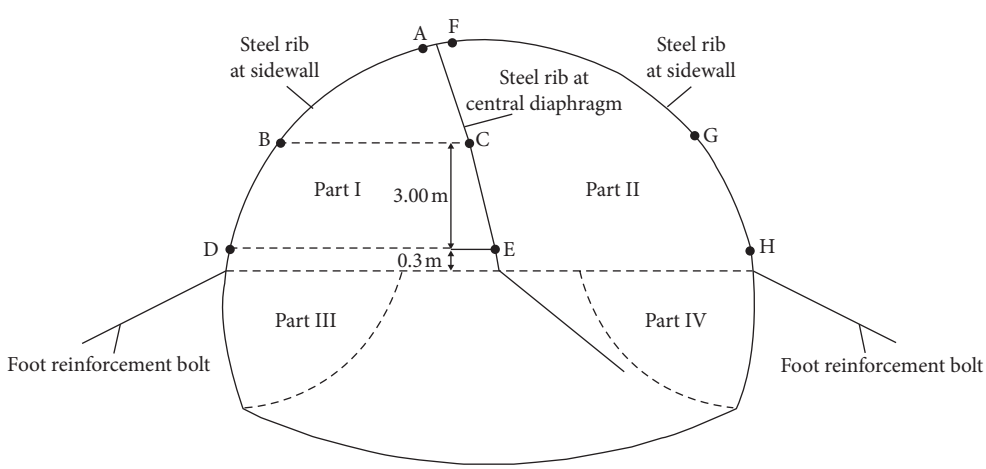

Figure 3: Layout of deformation measurement points in Wangcun tunnel.

Figure 4: Relative film.

Figure 5: Field measurement situation.

Table 2: The observation frequency in Wangcun tunnel.

Serial number	Item	Instrument	Observation frequency	
1	Horizontal convergence	Total station	1–15 days 16 days—1 month After 1 month	1-2 times/day 1 time/day 1-2 times/week
2	Crown settlement	Total station	1–15 days 16 days—1 month After 1 month	1-2 times/day 1 time/day 1-2 times/week

Table 3: The accumulated crown settlement value at the monitoring section in Wangcun tunnel.

Pile number	Vault (A) (mm)	Left arch waist (B) (mm)	Part I in the upper bench Central diaphragm waist (C) (mm)	Maximum excavation line position at left arch (D) (mm)	Maximum excavation line position at central diaphragm (E) (mm)
YK11 + 937	131	131	—	—	25
YK11 + 931	—	67	60	—	54
YK11 + 928	51	52	41	58	45
YK11 + 925	38	34	36	46	13
Pile number	Vault (F) (mm)	Right arch waist (G) (mm)	Part II in the upper bench Central diaphragm waist (C) (mm)	Maximum excavation line position at right arch (H) (mm)	Maximum excavation line position at central diaphragm (E) (mm)
YK11 + 937	35	53	—	40	25
YK11 + 931	24	43	60	65	54
YK11 + 928	21	23	41	36	45
YK11 + 925	19	16	36	19	13

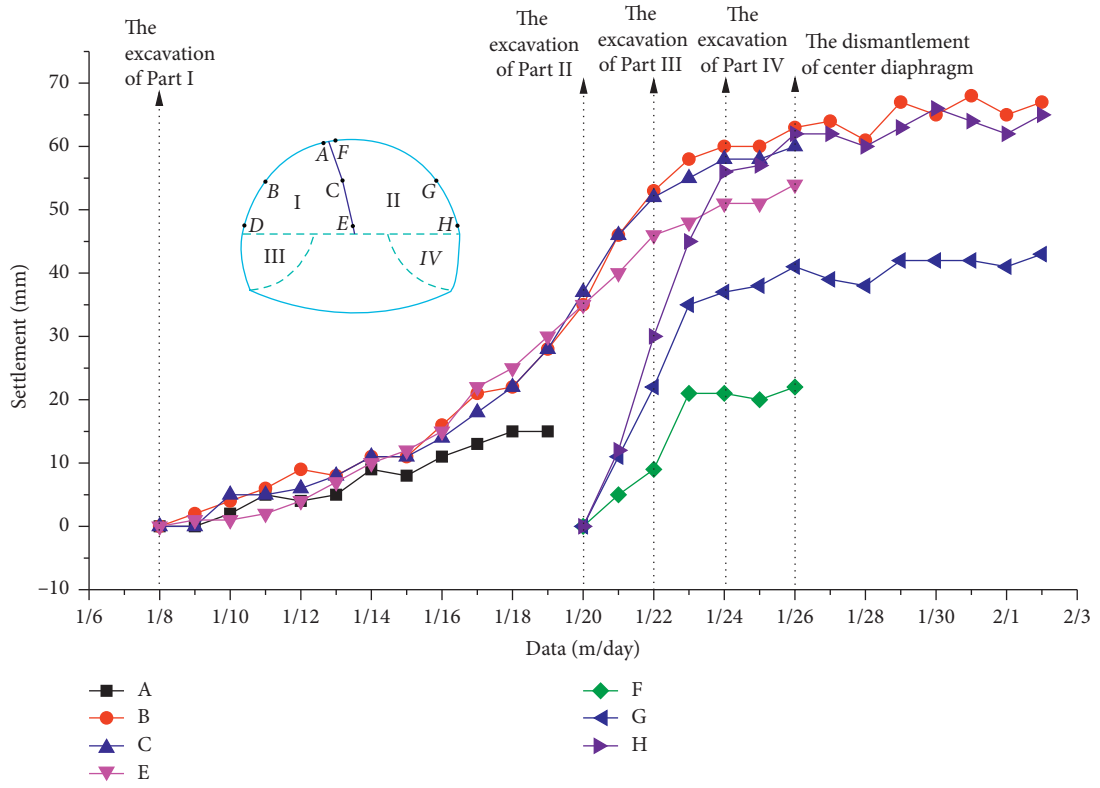

Figure 6: Crown settlement temporal curve at section YK11 + 931.

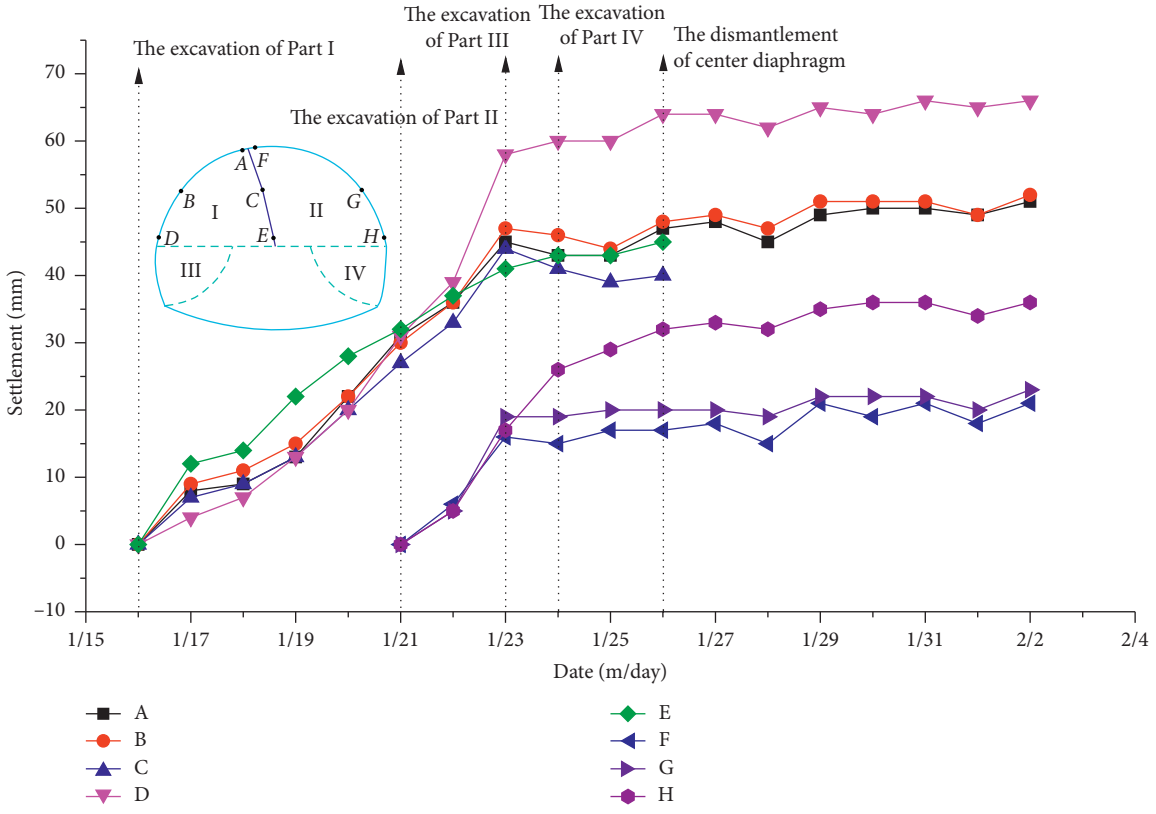

Figure 7: Crown settlement temporal curve at section YK11 + 928.

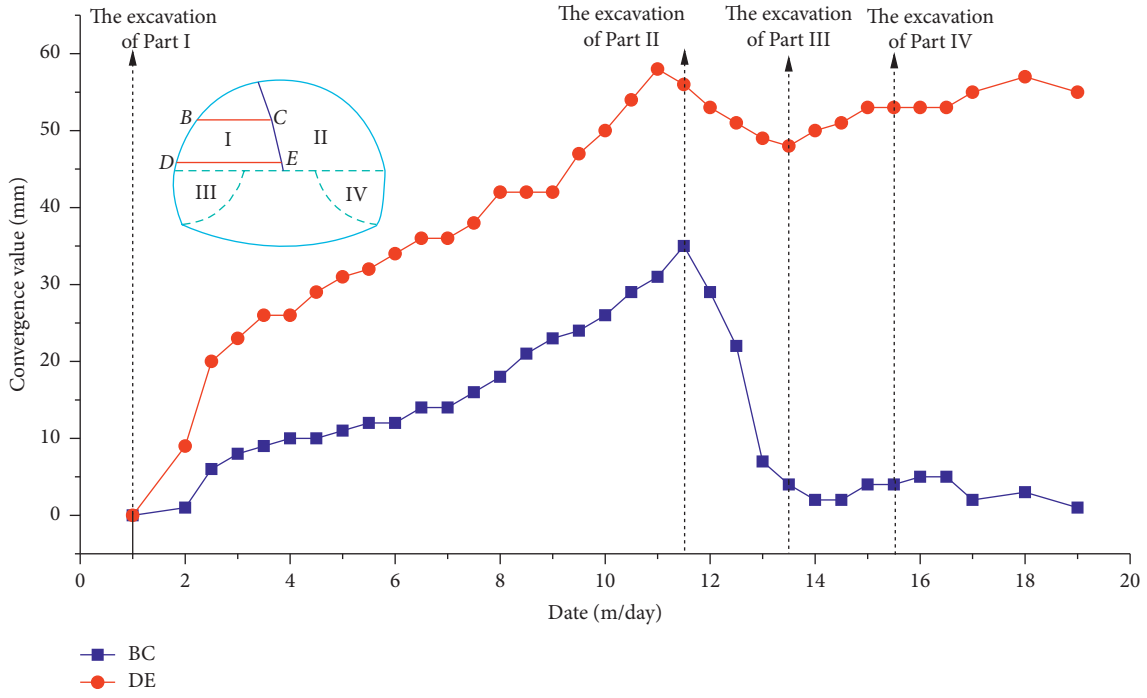

Figure 8: Horizontal convergence temporal curve at section YK11 + 931.

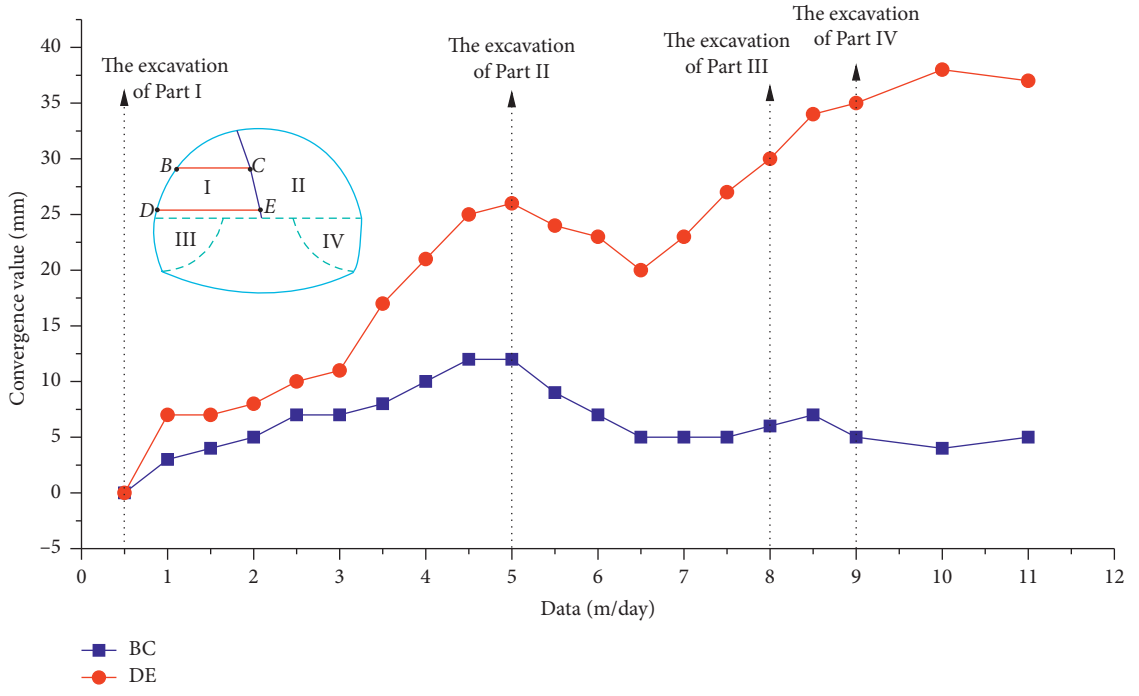

Figure 9: Horizontal convergence temporal curve at section YK11 + 928.

vault (*A*) and arch waist (*B*) at the sidewall steel rib in Part I meet the basically consistent change rule according to Figures 6 and 7, and the final cumulative settlement value is also basically the same, which shows that the settlement of sidewall steel rib arch part in Part I during the process of tunnel construction is the overall settlement. At the same time, the cumulative settlement value of sidewall steel rib (*A*, *B*, and *D*) in Part I is significantly greater than that of the sidewall steel rib (*F*, *G*, and *H*) in Part II. It can be concluded that the deformation response of support structure in Part I is more intense in the process of tunnel excavation, and the excavation of Part II influences the structure deformation of Part I. The settlement value of steel rib in the middle diaphragm is between 13 mm and 60 mm, and the settlement value at the middle diaphragm arch waist is slightly greater than that at the maximum excavation line. The accumulated

settlement value of each part at the support structure is less than the reserved deformation value of 150 mm specified in "Specifications for Design of Highway Tunnels" [34], and the maximum value is 131 mm but only appears at individual measuring points. The average cumulative settlement value of steel rib structure is 44.3 mm, accounting for 29.5% of reserved deformation value. At the same time, the field monitoring results show that there is no obvious deformation and cracking in all parts at the support structure. Therefore, it is not difficult to find out that the application of upper bench CD method in the construction of large-span loess tunnel is feasible, and the construction of this method can ensure the safety and stability of support structure.

Figures 6 and 7 show the typical settlement of sidewall steel rib and central diaphragm structure at YK11 + 931 and YK11 + 928 sections. With the construction of each excavation part in tunnel, the settlement value of monitoring point on the sidewall and the central diaphragm changed obviously, which shows the characteristics of increasing first and then gradually stabilizing. The maximum settlement values of YK11 + 928 and YK11 + 931 sections are 66 mm and 67 mm, respectively, which are located at the sidewall of Part I, respectively, at the arch foot and the arch waist. The maximum settlement rates at sections YK11 + 928 and YK11 + 931 are 8 mm/day and 14 mm/day, respectively. To be summarized, the settlement of each point mainly occurred in the excavation stage of upper bench (Parts I and II), and the settlement accounts for about 80% of the total deformation of YK11 + 928 section in this stage, while that of YK11 + 931 section is about 75%. The excavation of the lower part in tunnel (Parts III and IV) has little influence on the settlement of tunnel. After the excavation of Part IV and the installation of steel rib, the settlement gradually tends to be stable over time.

Based on the analysis of settlement variation at the central diaphragm waist and the maximum excavation line during the excavation of different parts in tunnel, it can be seen that the settlement caused by the excavation of Part I is 25–36 mm, with an average value of 31 mm, accounting for 58%–75% of the total settlement of central diaphragm; the settlement caused by the excavation of Part II is 10–18 mm, with an average value of 13 mm, accounting for 45%–17% of total settlement. It can be seen that the settlement ratio for waist and maximum excavation line position at the central diaphragm caused by the excavation of Part I is relatively large, that caused by the excavation of Part II is the second, and that caused by the excavation of Parts III and IV is small. The settlement of central diaphragm waist and maximum excavation line position at the research section after the excavation of Parts I and II account for about 90% of the total settlement before the removal of central diaphragm, which shows that the settlement located at the waist and maximum excavation line position of central diaphragm are mainly affected by the excavation of Parts I and II in upper bench.

Figures 8 and 9 show the horizontal convergence at the arch waist and the maximum excavation line position in Part I of tunnel at sections YK11 + 931 and YK11 + 928 during the construction by the upper bench CD method. Figure 8 shows that the convergence value of arch waist and the maximum excavation line position in Part I changed significantly during the tunnel construction at YK11 + 931 section. The maximum convergence values at the arch waist and the maximum excavation line position are 35 mm and 58 mm, respectively, both of which are less than 150 mm of reserved excavation deformation specified in the tunnel design and "Specifications for Design of Highway Tunnels." After the excavation of Part I, the convergence value at the two positions increased sharply, and the convergence value at the maximum excavation line position increased the most in the first three days, reaching 12 mm/day. The convergence value at the two positions reached the maximum before the excavation of Part II. After the excavation of Part II, the convergence values at the two positions decreased significantly. The convergence reduction values at the arch waist and the maximum excavation line position are 10 mm and 31 mm, respectively, and the convergence values of arch waist decreased the fastest, reaching 9 mm/day. After the excavation of Part 0049II, the convergence value at the maximum excavation line position increased to 53 mm gradually, and the convergence value at the arch waist slightly decreased to 2 mm and then slowly increased to 4 mm. After the excavation of Part IV and the installation of steel rib, the convergence value at the two positions stabilized gradually.

The horizontal convergence at the arch waist and the maximum excavation line position of section YK11 + 928 are similar to those of section YK11 + 931. The maximum convergence values at the arch waist and the maximum excavation line position are 12 mm and 38 mm, respectively. After the excavation of Part I, the horizontal convergence at the arch waist and the maximum excavation line position increased rapidly to 12 mm and 26 mm, respectively. Compared with the YK11 + 931 section, the time for the horizontal convergence of this section to increase to the maximum value was shorter. The convergence value at the maximum excavation line position increased the fastest from the 3rd to 4th day after excavation of Part I, reaching 11 mm/day. The convergence value at the two positions reached the maximum before the excavation of Part II. After the excavation of Part II, the convergence value of arch waist gradually reduced to 6 mm, and that of the maximum excavation line position first reduced to 20 mm and then increased to 30 mm. After the excavation of Part III, the convergence value at the maximum excavation line position continued to increase to 35 mm; the convergence value at the arch waist slightly increased and then decreased to 5 mm. After the excavation of Part IV, the convergence value at the maximum excavation line position slightly increased and then remained stable; the convergence value at the arch waist slightly decreased and then remained stable.

From Figures 8 and 9, it can be seen that the excavation of Parts I and II in tunnel has the greatest influence on the convergence at the arch waist and the maximum excavation line position of central diaphragm structure. The convergence of two positions increased sharply after the excavation of Part I, and that of the two positions decreased significantly after the Part II excavation. The change rule of horizontal convergence at the arch waist was similar to that at the maximum excavation line position. The maximum convergence value at the maximum excavation line

position is about 2.25 times that at the arch waist, and the convergence value at the arch waist is smaller than that at the maximum excavation line position as a whole. The convergence at the above two positions has experienced four stages of "convergence-expansion-convergence-gradual stability."

This phenomenon is mainly caused by the change of rock mass pressure on the central diaphragm and the displacement at the arch foot of steel rib. After the excavation of Part I, the steel rib of sidewall and central diaphragm were installed, both of which were firmly and rigidly connected at the vault. At this time, the steel rib of sidewall and central diaphragm shared the loads together and reached a stable state. In this stage, the inclined central diaphragm steel rib not only undertook the soil pressure from Part II, but also indirectly undertook the load transferred from the sidewall steel rib. After the excavation of Part II, the soil pressure in this part directly acting on the central diaphragm disappeared. In this stage, the inward horizontal elastic deformation of central diaphragm structure due to the disappearance of soil pressure in Part II was restored. At the same time, the soil contacted with the sidewall steel rib acted on the integral support structure composed of the steel rib of sidewall and central diaphragm, resulting in the outward elastic deformation in the central diaphragm structure. These two actions led to the outward expansion of central diaphragm structure, and then the horizontal convergence value decreased.

4. Mechanical Model for Support Structure

Engineering practice shows that the primary supporting structure of tunnel is generally composed of steel rib, shotcrete, anchor bolt, and steel mesh, and steel rib is the main bearing structure. According to the field engineering practice and the bearing mechanism of supporting structure, this paper only considers the deformation behaviors and mechanical properties of steel rib structure when studying the construction mechanical behavior of supporting structure in upper bench CD method.

After the excavation of Part I constructed by upper bench CD method, the sidewall steel rib and the middle diaphragm steel rib were constructed with the rigid connection at the arch crown. At the same time, the bottom of steel rib is firmly welded with the FRB, both of which are elastically fixed and deformed coordinately. After the excavation of Part II at the upper bench, the load caused by the rock mass in Part II acting on the middle diaphragm structure disappeared. The inward horizontal elastic deformation of central diaphragm structure due to the disappearance of soil pressure in Part II was restored. At the same time, the soil contacted with the sidewall steel rib acted on the integral support structure composed of the steel rib of sidewall and central diaphragm, resulting in the outward elastic deformation in the central diaphragm structure. According to the deformation and mechanical characteristics of support structure in the actual construction process, the excavation process and the bearing mode of support structure are shown in Figures 10 and 11, respectively.

The support system is regarded as the arch-beam fixed structure with three times of statically indeterminate and movable abutment in this mechanical model. The model structure satisfies the following assumptions: (1) sidewall steel rib is regarded as the arc structure with equal radius; (2) the central diaphragm steel rib is regarded as the beam structure, which is erected along the radius direction of arc structure; and (3) the whole model is rigidly connected at each node.

The calculation model is shown in Figure 12. The arch structure and beam structure in the calculation model are shown in Figures 13 and 14, respectively, where q is the uniform load acting on the supporting structure; e_1, e_2 are the horizontal side pressure acting on the supporting structure; f is the excavation height of Part I; β_1 and β_2 are the corner of arch foot section in the sidewall steel rib and the central diaphragm steel rib, respectively; ν_1 and ν_2 are the vertical displacement of arch foot section in the sidewall steel rib and the central diaphragm steel rib respectively; μ_1 and μ_2 are the horizontal displacement of arch foot section in the sidewall steel rib and the central diaphragm steel rib, respectively; α is the angle between the central diaphragm and the horizontal direction; and l_1 and l_2 are the horizontal projection length of sidewall steel rib and central diaphragm steel rib, respectively.

The whole model structure is symmetric and the load distribution is asymmetric, so there is shear force at the top rigid joint of sidewall steel rib and the central diaphragm steel rib. The structural forces X_1, X_2, and X_3 at the top rigid joint of model are solved by the force method of structural mechanics, where X_1 is the bending moment of steel rib at the top joint, X_2 is the axial force of steel rib at the top joint, and X_3 is the shear force of steel rib at the top joint. The positive direction of each structural internal force in arch structure and beam structure is shown in Figures 13 and 14, respectively. According to the analysis of structural characteristics, it can be concluded that the relative rotation angle, relative axial displacement, and relative radial displacement at the section of top rigid joint are all equal to 0. Figure 15 shows the basic calculation system of model structure. The displacement coordination equation of model structure is shown in the following equation:

$$\begin{cases} X_1\delta_{11} + X_2\delta_{12} + \Delta_{1p} + (\beta_1 + \beta_2) = 0, \\ X_1\delta_{21} + X_2\delta_{22} + \Delta_{2p} + (\mu_1 + \mu_2)\sin\alpha + (\nu_1 + \nu_2)\cos\alpha + f(\beta_1 + \beta_2)\sin\alpha + (l_2\beta_2 - l_1\beta_1)\cos\alpha = 0, \\ X_3\delta_{33} + \Delta_{3p} - (\mu_1 + \mu_2)\cos\alpha + (\nu_1 + \nu_2)\sin\alpha - f(\beta_1 + \beta_2)\cos\alpha + (l_2\beta_2 - l_1\beta_1)\sin\alpha = 0. \end{cases} \quad (1)$$

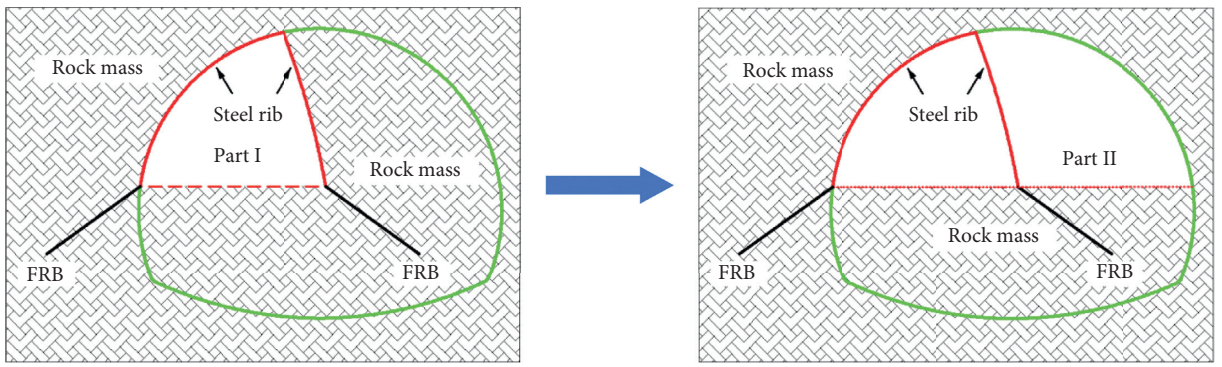

Figure 10: Schematic diagram of excavation for Part I and Part II.

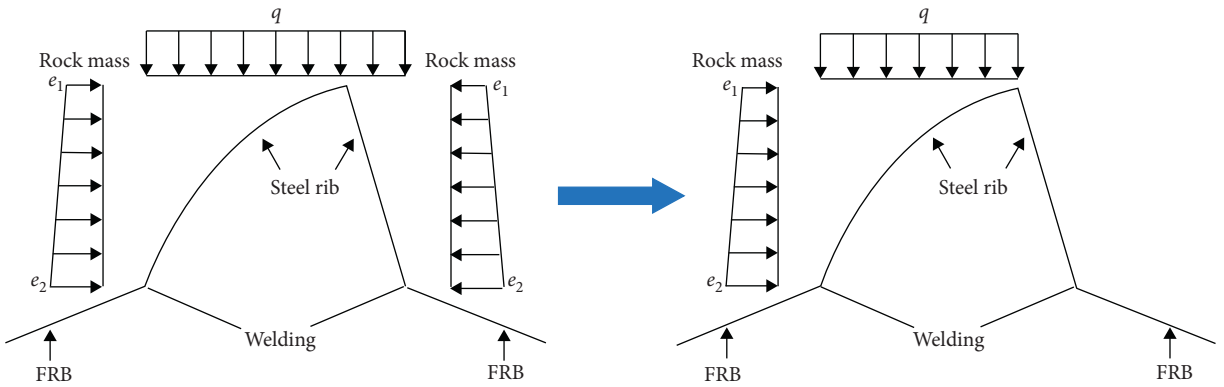

Figure 11: Bearing mode of supporting structure.

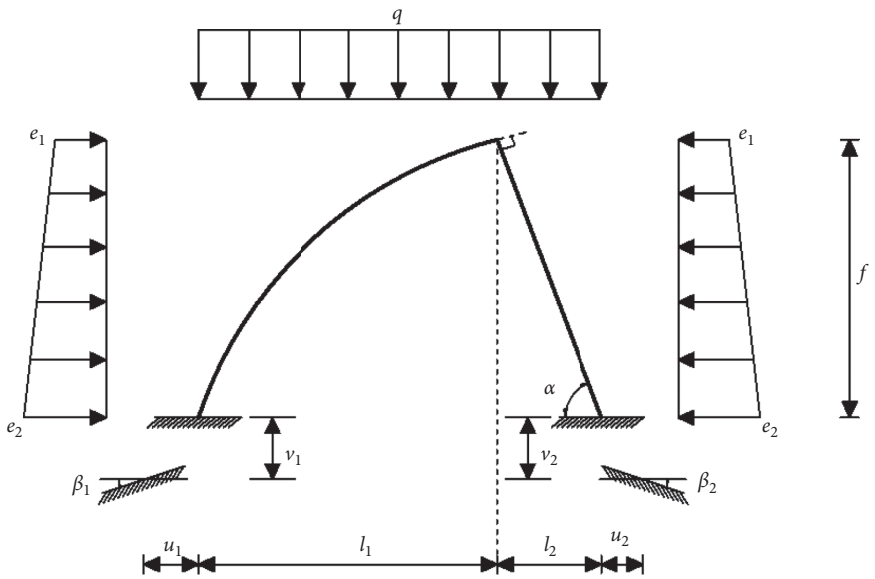

Figure 12: Support model of leading upper bench by the upper bench CD method.

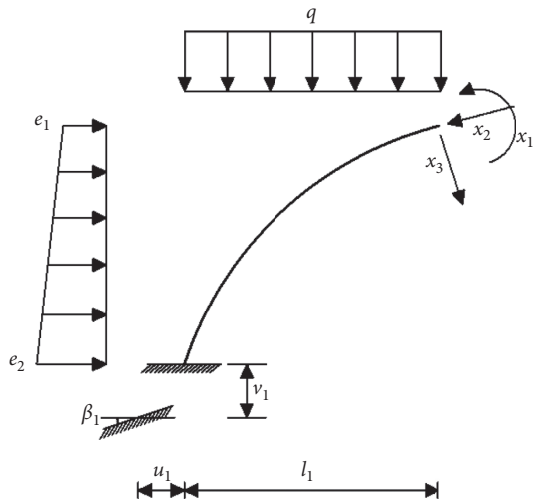

Figure 13: Arch structure model.

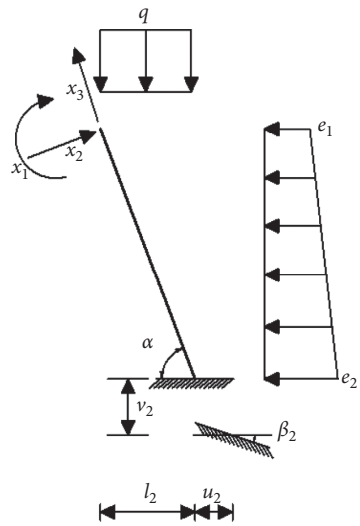

Figure 14: Beam structure model.

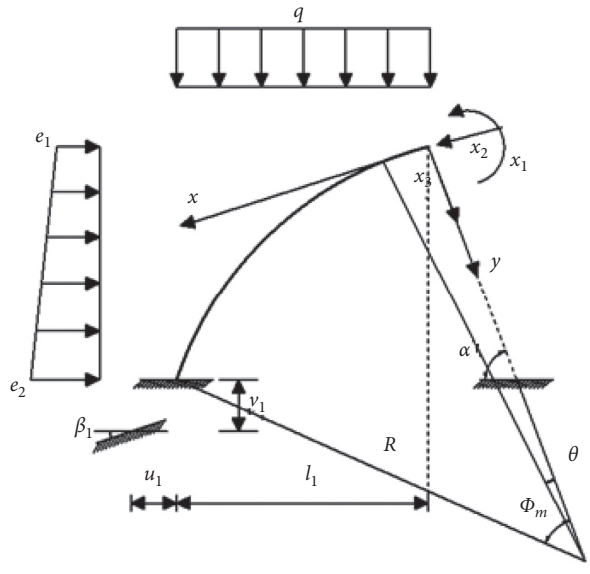

Figure 15: Basic calculation system of model by force method.

From Figure 15, it can be concluded that the coefficients value in the previous equation meets the following conditions:

$$\left.\begin{aligned}
\beta_1 &= X_1\beta_{11} + X_2\left[\beta_{21} + \left(\frac{f-l_1}{\tan\alpha}\right)\sin\alpha\beta_{11}\right] + X_3\left[\beta_{31} - (l_1+l_2)\sin\alpha\beta_{11}\right] + \beta_{p1}\\
\beta_2 &= X_1\beta_{12} + X_2\left[\beta_{22} + \left(\frac{f}{\sin\alpha}\right)\beta_{12}\right] + X_3\beta_{32} + \beta_{p2}\\
\mu_1 &= X_1\mu_{11} + X_2\left[\mu_{21} + \left(\frac{f-l_1}{\tan\alpha}\right)\sin\alpha\mu_{11}\right] + X_3\left[\mu_{31} - (l_1+l_2)\sin\alpha\mu_{11}\right] + \mu_{p1}\\
\mu_2 &= X_1\mu_{12} + X_2\left[\mu_{22} + \left(\frac{f}{\sin\alpha}\right)\mu_{12}\right] + X_3\mu_{32} + \mu_{p2}\\
\nu_1 &= X_1\nu_{11} + X_2\left[\nu_{21} + \left(\frac{f-l_1}{\tan\alpha}\right)\sin\alpha\nu_{11}\right] + X_3\left[\nu_{31} - (l_1+l_2)\sin\alpha\nu_{11}\right] + \nu_{p1}\\
\nu_2 &= X_1\nu_{12} + X_2\left[\nu_{22} + \left(\frac{f}{\sin\alpha}\right)\nu_{12}\right] + X_3\nu_{32} + \nu_{p2}
\end{aligned}\right\}. \tag{2}$$

The bottom of steel rib is firmly welded with the FRB. According to the Winkler foundation beam model [35–37] and the elastic foundation beam theory [38], the unit displacement and load displacement at the foot of sidewall steel rib and the central diaphragm steel rib can be calculated by the following two equations, respectively:

$$\left\{\begin{aligned}
\beta_{11} &= \frac{4\alpha_1^3}{KD_1},\\
\mu_{11} = \beta_{21} &= \frac{2\alpha_1^2}{KD_1}\sin\theta_1,\\
\mu_{21} &= \frac{2\alpha_1}{KD_1}\sin^2\theta_1,\\
\nu_{11} = \beta_{31} &= -\frac{2\alpha_1^2}{KD_1}\cos\theta_1,\\
\nu_{21} = \mu_{31} &= -\frac{\alpha_1}{KD_1}\sin 2\theta_1,\\
\nu_{31} &= \frac{2\alpha_1}{KD_1}\cos^2\theta_1,\\
\beta_{p1} &= \frac{2\alpha_1^2}{KD_1}\left(2\alpha_1 M_{p1} + Q_{p1}\right),\\
\mu_{p1} &= \frac{2\alpha_1}{KD_1}\left(\alpha_1 M_{p1} + Q_{p1}\right)\sin\theta_1,\\
\nu_{p1} &= -\frac{2\alpha_1}{KD_1}\left(\alpha M_{p1} + Q_{p1}\right)\cos\theta_1,
\end{aligned}\right. \tag{3}$$

$$\left\{\begin{aligned}
\beta_{12} &= \frac{4\alpha_3^2}{KD_2},\\
\mu_{12} = \beta_{22} &= \frac{2\alpha_2^2}{KD_2}\sin\theta_2,\\
\mu_{22} &= \frac{2\alpha_2}{KD_2}\sin^2\theta_2,\\
\nu_{12} = \beta_{32} &= \frac{2\alpha_2^2}{KD_2}\cos\theta_2,\\
\nu_{22} = \mu_{32} &= \frac{\alpha_2}{KD_2}\sin 2\theta_2,\\
\nu_{32} &= \frac{2\alpha_2}{KD_2}\cos^2\theta_2,\\
\beta_{p2} &= \frac{2\alpha_2^2}{KD_2}\left(2\alpha_2 M_{p2} + Q_{p2}\right),\\
\mu_{p2} &= \frac{2\alpha_2}{KD_2}\left(\alpha_2 M_{p2} + Q_{p2}\right)\sin\theta_2,\\
\nu_{p2} &= \frac{2\alpha_2}{KD_2}\left(\alpha_2 M_{p2} + Q_{p2}\right)\cos\theta_2.
\end{aligned}\right. \tag{4}$$

M_{pi} and Q_{pi} can be obtained from the following equation:

$$\begin{aligned}
M_{p1} &= -q\cdot l_1\cdot\frac{1}{2}l_1 - e_1\cdot f\cdot\frac{1}{2}f - \int_0^f \frac{x}{f}(e_2-e_1)(f-x)\mathrm{d}x,\\
Q_{p1} &= -ql_1\cos\theta_1 - \left[e_1\cdot f + \int_0^f \frac{x}{f}(e_2-e_1)\mathrm{d}x\right]\sin\theta_1,\\
M_{p2} &= -q\cdot l_2\cdot\frac{1}{2}l_2 - e_1\cdot f\cdot\frac{1}{2}f - \int_0^f \frac{x}{f}(e_2-e_1)(f-x)\mathrm{d}x,\\
Q_{p2} &= -ql_2\cos\theta_2 - \left[e_1\cdot f + \int_0^f \frac{x}{f}(e_2-e_1)\mathrm{d}x\right]\sin\theta_2,
\end{aligned} \tag{5}$$

where β_{11}, β_{12}, μ_{11}, μ_{12}, ν_{11}, and ν_{12} are the angle, horizontal displacement, and vertical displacement of structure bottom caused by the unit moment acting on the foot of sidewall steel rib and the central diaphragm steel rib; β_{21}, β_{22}, μ_{21}, μ_{22}, and ν_{21} are the angle, horizontal displacement, and vertical displacement of structure bottom caused by the unit horizontal force acting on the foot of sidewall steel rib and central diaphragm steel rib; β_{31}, β_{32}, μ_{31}, μ_{32}, ν_3, and ν_{32} are the angle, horizontal displacement, and vertical displacement of structure bottom caused by the unit vertical force acting on the foot of sidewall steel rib and the central diaphragm steel rib; β_{p1}, β_{p2}, μ_{p1}, μ_{p2}, ν_{p1}, and ν_{p2} are the angle, horizontal displacement, and vertical displacement of structure bottom in the sidewall steel rib and the central diaphragm steel rib of basic structure under the action of rock mass pressure; θ_1, θ_2 are the setting angle of FRB at the foot of sidewall steel rib and central diaphragm steel rib, respectively; M_{p1}, M_{p2}, Q_{p1}, and Q_{p2} are the bending moment and shear force at the foot of sidewall steel rib and central diaphragm steel rib under the surrounding rock load, respectively; and α_1 and α_2 are the deformation coefficient of FRB at the structure bottom of sidewall steel rib and the central diaphragm steel rib, respectively; $\alpha = \sqrt[4]{KD/4E_dI_z}$, K is the elastic resistance coefficient of rock mass, D is the borehole diameter, $E_dI_z = 2\times(E_sI_s + E_gI_g)$, and E_s, I_s, E_g, and I_g is the elastic modulus (Pa) and inertia moment of cross-section (m^4) of bolt and mortar, respectively.

δ_{ik} is the flexibility coefficient, which represents the displacement ($i, k = 1, 2, 3$) generated along the structural forces X_i direction when unit force $X_K = 1$ acts on the cantilever end of steel rib in the basic structure; according to the structural characteristics of model, $\delta_{13} = \delta_{31} = \delta_{23} = \delta_{32} = 0$; according to Figure 15, the displacement δ_{ik} can be calculated according to the following equations:

$$\delta_{11} = \int \frac{1}{E_sI_s}\mathrm{d}_s = \frac{1}{E_sI_s}\int_0^{\varphi_m} R\mathrm{d}\theta + \frac{1}{E_sI_s}\int_0^{f/\sin\alpha} 1\mathrm{d}s = \frac{1}{E_sI_s}\left(R\varphi_m + \frac{f}{\sin\alpha}\right), \tag{6}$$

$$\begin{aligned}\delta_{12} = \delta_{21} &= \int \frac{y}{E_sI_s}\mathrm{d}s = \frac{1}{E_sI_s}\int_0^{\varphi_m}(R - R\cos\theta)R\mathrm{d}\theta + \frac{1}{E_sI_s}\int_0^{f/\sin\alpha} s\mathrm{d}s \\ &= \frac{1}{2E_sI_s}\left[2R^2(\varphi_m - \sin\varphi_m) + \frac{f^2}{\sin^2\alpha}\right],\end{aligned} \tag{7}$$

$$\begin{aligned}\delta_{22} &= \int \frac{y^2}{E_sI_s}\mathrm{d}s = \frac{1}{E_sI_s}\int_0^{\varphi_m}(R - R\cos\theta)^2 R\mathrm{d}\theta + \frac{1}{E_sI_s}\int_0^{f/\sin\alpha} s^2\mathrm{d}s \\ &= \frac{R^3}{E_sI_s}\int_0^{\varphi_m}\left(1 + \cos^2\theta - 2\cos\theta\right)\mathrm{d}\theta + \frac{1}{E_sI_s}\int_0^{f/\sin\alpha} s^2\mathrm{d}s \\ &= \frac{1}{6E_sI_s}\left[3R^3\left(3\varphi_m - 4\sin\varphi_m + \frac{1}{2}\sin 2\varphi_m\right) + 2\frac{f^3}{\sin^3\alpha}\right],\end{aligned} \tag{8}$$

$$\delta_{33} = \int \frac{x^2}{E_sI_s}\mathrm{d}s = \frac{1}{E_sI_s}\int_0^{\varphi_m}(R\sin\theta)^2 R\mathrm{d}\theta = \frac{R^3}{2E_sI_s}\left(\varphi_m - \frac{1}{2}\sin 2\varphi_m\right). \tag{9}$$

Δ_{ip} is the displacement ($i = 1, 2, 3$) generated along the direction of structural forces X_i under the action of rock mass pressure in the basic structure; according to the structural displacement calculation model (Figure 15), the displacement Δ_{ip} can be calculated according to the following equations:

$$\begin{aligned}\Delta_{1p} = \int \frac{M_p}{E_sI_s}\mathrm{d}s &= -\int_0^{\varphi_m}\frac{[R\sin\theta\sin\alpha - (R - R\cos\theta)\cos\alpha]^2 qR}{2E_sI_s}\mathrm{d}\theta \\ &- \int_0^{\varphi_m}\frac{[R\sin\theta\cos\alpha + (R - R\cos\theta)\sin\alpha]^2\cdot e_1 R}{2E_sI_s}\mathrm{d}\theta \\ &- \int_0^{\varphi_m}\frac{[R\sin\theta\cos\alpha + (R - R\cos\theta)\sin\alpha]^3\cdot(e_2 - e_1)(1/3)R}{2E_sI_sf}\mathrm{d}\theta \\ &- \int_0^{f/\sin\alpha}\frac{q\cos\alpha\cdot x^2}{2E_sI_s}\mathrm{d}x - \int_0^{f/\sin\alpha}\frac{e_1\sin\alpha\cdot x^2}{2E_sI_s}\mathrm{d}x - \int_0^{f/\sin\alpha}\frac{(e_2 - e_1)\sin\alpha\cdot x^2(1/3)x}{2E_sI_sf/\sin\alpha}dx,\end{aligned} \tag{10}$$

$$\begin{aligned}\Delta_{2p} = \int \frac{yM_p}{E_sI_s}\mathrm{d}s &= -\int_0^{\varphi_m} \frac{(R - R\cos\theta)[R\sin\theta\sin\alpha - (R - R\cos\theta)\cos\alpha]^2 qR}{2E_sI_s}\mathrm{d}\theta \\ &- \int_0^{\varphi_m} \frac{(R - R\cos\theta)[R\sin\theta\cos\alpha + (R - R\cos\theta)\sin\alpha]^2 \cdot e_1 R}{2E_sI_s}\mathrm{d}\theta \\ &- \int_0^{\varphi_m} \frac{(R - R\cos\theta)[R\sin\theta\cos\alpha + (R - R\cos\theta)\sin\alpha]^3 \cdot (e_2 - e_1)(1/3)R}{2E_sI_sf}\mathrm{d}\theta \\ &- \int_0^{f/\sin\alpha} \frac{q\cos\alpha \cdot x^3}{2E_sI_s}\mathrm{d}x - \int_0^{f/\sin\alpha} \frac{e_1\sin\alpha \cdot x^3}{2E_sI_s}\mathrm{d}x - \int_0^{f/\sin\alpha} \frac{(e_2 - e_1)\sin\alpha \cdot x^2(1/3)x^2}{2E_sI_sf/\sin\alpha}\,dx,\end{aligned} \tag{11}$$

$$\begin{aligned}\Delta_{3p} = \int \frac{xM_p}{E_sI_s}\mathrm{d}s &= \int_0^{\varphi_m} \frac{R\sin\theta[R\sin\theta\sin\alpha - (R - R\cos\theta)\cos\alpha]^2 qR}{2E_sI_s} \\ &+ \int_0^{\varphi_m} \frac{R\sin\theta[R\sin\theta\cos\alpha + (R - R\cos\theta)\sin\alpha]^2 \cdot e_1 R}{2E_sI_s}\mathrm{d}\theta \\ &+ \int_0^{\varphi_m} \frac{R\sin\theta[R\sin\theta\cos\alpha + (R - R\cos\theta)\sin\alpha]^3 \cdot (e_2 - e_1)(1/3R)}{2E_sI_sf}\,dx,\end{aligned} \tag{12}$$

where φ_m is the central angle corresponding to the arc of steel rib; R is the radius of arc; and E_sI_s is the compressive stiffness of steel rib (N·m^2). The model structure satisfies the following geometric relations:

$$\frac{l_1 + l_2 + (R - f/\sin\alpha)\cos\alpha}{\tan((\pi/2) + \varphi_m - \alpha)} = (R - f/\sin\alpha)\sin\alpha. \tag{13}$$

According to equation (1), the linear equations of structure forces X_1, X_2, and X_3 can be transformed into the following equation:

$$\begin{cases} a_{11}X_1 + a_{12}X_2 + a_{13}X_3 + a_{10} = 0, \\ a_{21}X_1 + a_{22}X_2 + a_{23}X_3 + a_{20} = 0, \\ a_{31}X_1 + a_{32}X_2 + a_{33}X_3 + a_{30} = 0. \end{cases} \tag{14}$$

By substituting β_{ik} and μ_{ik} obtained from (3) and (4) and the displacements δ_{ik} and Δ_{ip} of basic structure obtained from (6)–(12) into (1), the calculation formulas of a_{ik} are shown in the following equations

:

$$\begin{aligned} a_{11} &= \delta_{11} + (\beta_{11} + \beta_{12}), \\ a_{12} &= \delta_{12} + \left[\beta_{21} + \left(\frac{f - l_1}{\tan\alpha}\right)\sin\alpha\beta_{11} + \beta_{22} + \left(\frac{f}{\sin\alpha}\right)\beta_{12}\right], \\ a_{13} &= \beta_{31} - (l_1 + l_2)\sin\alpha\beta_{11} + \beta_{32}, \\ a_{10} &= \Delta_{1p} + \beta_{p1} + \beta_{p2}, \end{aligned} \tag{15}$$

$$a_{21} = \delta_{21} + (\mu_{11} + \mu_{12})\sin\alpha + (\nu_{11} + \nu_{12})\cos\alpha + f(\beta_{11} + \beta_{12})\sin\alpha + (l_2\beta_{12} - l_1\beta_{11})\cos\alpha, \tag{16}$$

$$\begin{aligned} a_{22} = \delta_{22} &+ \left[\mu_{21} + \left(\frac{f - l_1}{\tan\alpha}\right)\sin\alpha\mu_{11} + \mu_{22} + \left(\frac{f}{\sin\alpha}\right)\mu_{12}\right]\sin\alpha \\ &+ \left[\nu_{21} + \left(\frac{f - l_1}{\tan\alpha}\right)\sin\alpha\nu_{11} + \nu_{22} + \left(\frac{f}{\sin\alpha}\right)\nu_{12}\right]\cos\alpha \\ &+ f\left[\beta_{21} + \left(\frac{f - l_1}{\tan\alpha}\right)\sin\alpha\beta_{11} + \beta_{22} - \left(\frac{f}{\sin\alpha}\right)\beta_{12}\right]\sin\alpha \\ &+ \left[l_2\beta_{22} + l_2\left(\frac{f}{\sin\alpha}\right)\beta_{12} + l_1\beta_{21} - l_1\left(\frac{f - l_1}{\tan\alpha}\right)\sin\alpha\beta_{11}\right]\cos\alpha, \end{aligned} \tag{17}$$

$$
\begin{aligned}
a_{23} &= [\mu_{31} - (l_1 + l_2)\sin\alpha\mu_{11} + \mu_{32}]\sin\alpha + [\nu_{31} - (l_1 + l_2)\sin\alpha\nu_{11} + \nu_{32}]\cos\alpha + \\
&\quad f[\beta_{31} - (l_1 + l_2)\sin\alpha\beta_{11} + \beta_{32}]\sin\alpha + [l_2\beta_{32} - l_1\beta_{31} + l_1(l_1 + l_2)\sin\alpha\beta_{11}]\cos\alpha, \\
a_{20} &= \Delta_{2p} + (\mu_{p1} + \mu_{p2})\sin\alpha + (\nu_{p1} + \nu_{p2})\cos\alpha + f(\beta_{p1} + \beta_{p2})\sin\alpha + (l_2\beta_{p2} - l_1\beta_{p1})\cos\alpha,
\end{aligned} \tag{18}
$$

$$
\begin{aligned}
a_{31} &= -(\mu_{11} + \mu_{12})\cos\alpha + (\nu_{11} + \nu_{12})\sin\alpha - f(\beta_{11} + \beta_{12})\cos\alpha + (l_2\beta_{12} - l_1\beta_{11})\sin\alpha, \\
a_{32} &= -\left[\mu_{21} + \left(\frac{f - l_1}{\tan\alpha}\right)\sin\alpha\mu_{11} + \mu_{22} + \left(\frac{f}{\sin\alpha}\right)\mu_{12}\right]\cos\alpha + \left[\nu_{21} + \left(\frac{f - l_1}{\tan\alpha}\right)\sin\alpha\nu_{11} + \nu_{22} + \left(\frac{f}{\sin\alpha}\right)\nu_{12}\right]\sin\alpha - \\
&\quad f\left[\beta_{12} + \left(\frac{f - l_1}{\tan\alpha}\right)\sin\alpha\beta_{11} + \beta_{22} + \left(\frac{f}{\sin\alpha}\right)\beta_{12}\right]\cos\alpha + \left[l_2\beta_{22} + l_2\left(\frac{f}{\sin\alpha}\right)\beta_{12} - l_1\beta_{21} - l_1\left(\frac{f - l_1}{\tan\alpha}\right)\sin\alpha\beta_{11}\right]\sin\alpha,
\end{aligned} \tag{19}
$$

$$
\begin{aligned}
a_{33} &= \delta_{33} - [\mu_{31} - (l_1 + l_2)\sin\alpha\mu_{11} + \mu_{32}]\cos\alpha + [\nu_{31} - (l_1 + l_2)\sin\alpha\nu_{11} + \nu_{32}]\sin\alpha \\
&\quad - f[\beta_{31} - (l_1 + l_2)\sin\alpha\beta_{11} + \beta_{32}]\cos\alpha + [l_2\beta_{32} - l_1\beta_{31} + l_1(l_1 + l_2)\sin\alpha\beta_{11}]\sin\alpha, \\
a_{30} &= \Delta_{3p} - (\mu_{p1} + \mu_{p2})\cos\alpha + (\nu_{p1} + \nu_{p2})\sin\alpha - f(\beta_{p1} + \beta_{p2})\cos\alpha + (l_2\beta_{p2} - l_1\beta_{p1})\sin\alpha.
\end{aligned} \tag{20}
$$

5. Deformation Analysis of Support Structure by the Mechanical Model

5.1. Horizontal Deformation of Central Diaphragm Caused by Part II Loads. Figures 8 and 9 show that the convergence value of Part I decreased sharply after the excavation of Part II. In this stage, the main reason is that the rock mass originally acting on the central diaphragm structure in Part II was excavated, which led to the disappearance of load from the soil in Part II. The convergence reduction value in Part I corresponded to the horizontal deformation of central diaphragm structure under the above disappeared load. After the excavation of Part I, according to Figure 14, the bending moment at each position of central diaphragm steel rib can be calculated as shown in (21). After the excavation of Part II, for the arch-beam fixed structure, only the rock mass pressure acting on the sidewall steel rib in Part I is considered and the uniform load and horizontal load acting on the central diaphragm are 0, and the rock mass load q, e_1, and e_2 acting on the middle diaphragm disappear in Figure 12. According to Figure 11 and (4), β_{P2}, μ_{P2}, and ν_{P2} at the arch foot of middle diaphragm steel rib under the action of rock mass load in Part II are all 0, and the structure forces X_1', X_2', and X_3' for arch-beam fixed structure can be obtained according to (1)–(20). Then according to (21), the bending moment at each position of central diaphragm steel rib after the excavation of Part II can be calculated:

$$
\begin{aligned}
M(x) &= -X_1 + X_2 \cdot x - q \cdot \cos\alpha \cdot \frac{1}{2}x^2 \\
&\quad - e_1 \sin\alpha \cdot \frac{1}{2}x^2 - (e_2 - e_1)\sin\alpha \cdot \frac{x^3}{6}\,\frac{1}{f/\sin\alpha}.
\end{aligned} \tag{21}
$$

The relationship between bending moment and deflection is shown in the following equation:

$$
\frac{d^2\omega_l}{dx^2} = \frac{M(x)}{EI}. \tag{22}
$$

The deformation of central diaphragm structure can be obtained by double integration of bending moment, as shown in the following equations:

$$
\omega_l \cdot EI = \int\int [M(x)\mathrm{d}x]\mathrm{d}x + P_1 x + D_1, \tag{23}
$$

$$
\begin{aligned}
\omega_l \cdot EI &= -X_1 \cdot \frac{1}{2}x^2 + X_2 \cdot \frac{1}{6}x^3 - \frac{q}{2}\cos\alpha \cdot \frac{x^4}{12} \\
&\quad - \frac{e_1}{2}\sin\alpha \cdot \frac{x^4}{12} - (e_2 - e_1)\sin\alpha \\
&\quad \cdot \frac{1}{6 \cdot f/\sin\alpha} \cdot \frac{x^5}{20} + P_1 x + D_1.
\end{aligned} \tag{24}
$$

From Figures 6 and 7, P_1 and D_1 can be obtained according to the crown settlement values at positions C and E of central diaphragm and (23). The difference between the deformation value of middle diaphragm structure after the excavation of Part I and the deformation value after the excavation of Part II is the deformation influence value for middle diaphragm under the condition of Part II excavation. According to the field measured engineering data and the above formulas, the horizontal deformation of central diaphragm at the sections YK11 + 928 and YK11 + 931 influenced by Part II can be calculated as shown in Figure 16.

It can be seen from Figure 16 that the deformation for central diaphragm caused by the excavation of Part II is characterized by large deformation near the arch waist, small deformation at both ends, and larger deformation at the arch foot than that at the vault. The maximum horizontal deformation at sections YK11 + 928 and YK11 + 931 is 8.7 mm and 33.9 mm, respectively, which appears near the height of 3.35 m and 3.41 m, respectively. Relative errors for horizontal deformation of central diaphragm are illustrated in Table 4.

5.2. Horizontal Convergence Value in Part I. Considering the rock mass pressure acting on the sidewall steel rib and the central diaphragm during the excavation of Part I, a_{ik} can be

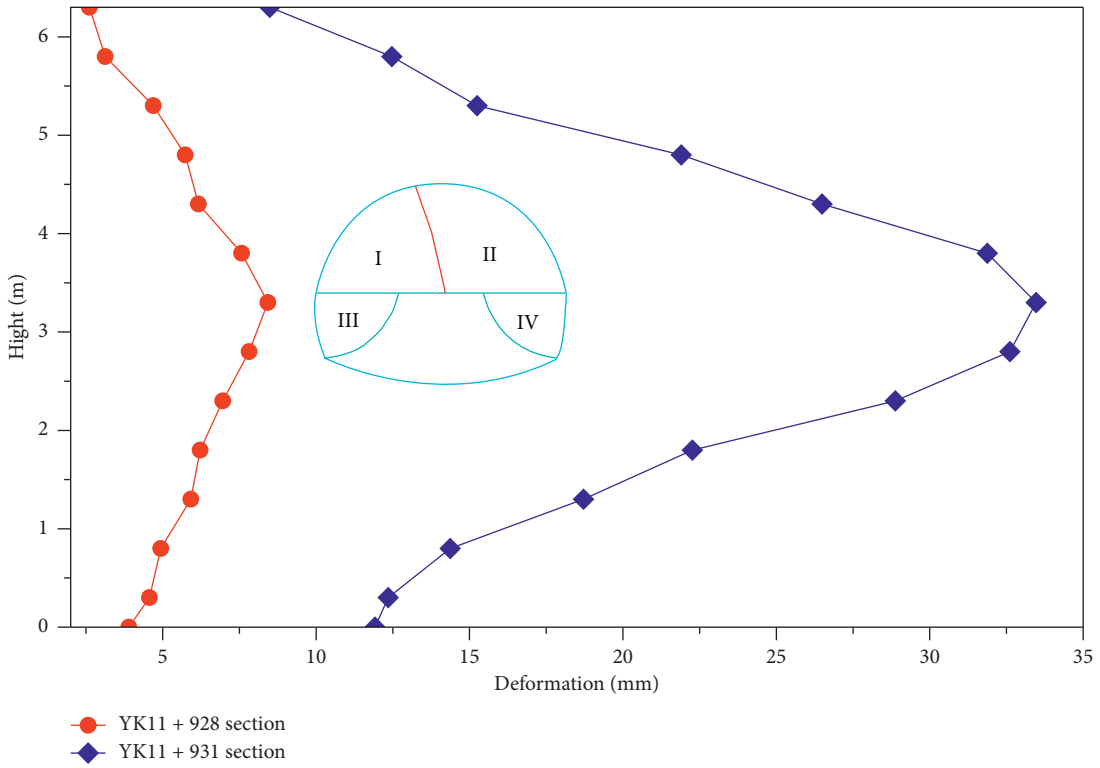

Figure 16: Horizontal deformation of central diaphragm caused by the excavation of Part II.

Table 4: Relative errors for horizontal deformation of central diaphragm.

Section pile number	Location of measuring points	Model calculation value (mm)	Field monitoring value (mm)	Relative error
YK11 + 931	Arch waist	33.5	28.0	19.6
	Maximum excavation line position	12.3	10.0	23.0
YK11 + 928	Arch waist	8.4	7.0	20.0
	Maximum excavation line position	4.6	6.0	23.3

obtained according to the measured values of each parameter and (1)–(20). Then the structure forces X_1, X_2, and X_3 for arch-beam rigid fixed structure can be obtained by combining a_{ik} with (14), and then the bending moment of sidewall steel rib can be calculated by the following equation:

$$M(\theta) = X_1 + X_2 \cdot (R - R\cos\theta) - X_3 \cdot R\sin\theta - \frac{1}{2} \cdot [R\sin\theta\sin\alpha - (R - R\cos\theta)\cos\alpha]^2 q - \frac{1}{2} \cdot [R\sin\theta\cos\alpha + (R - R\cos\theta)\sin\alpha]^2 e_1 - \frac{1}{6f} \cdot [R\sin\theta\cos\alpha + (R - R\cos\theta)\sin\alpha]^3 (e_2 - e_1). \quad (25)$$

The horizontal deformation of sidewall arch structure ω_H can be obtained by the following equations:

$$\omega_H = \omega_g(\theta) \cdot \cos(\theta - \alpha), \quad (26)$$

$$\frac{d^2\omega_H}{d\theta^2} = \frac{d^2\omega_g}{d\theta^2} \cdot \cos(\theta - \alpha) - 2\frac{d\omega_g}{d\theta} \cdot \sin(\theta - \alpha) - \omega \cdot \cos(\theta - \alpha), \quad (27)$$

$$\omega_g \cdot EI = \int\int [M(\theta)\mathrm{d}x]\mathrm{d}x + P_2 x + D_2. \quad (28)$$

From Figures 6 and 7, P_2 and D_2 can be obtained according to the crown settlement values at positions B and D of central diaphragm and (28). The horizontal convergence of Part I in tunnel is the superposition of deformation for sidewall steel rib and central diaphragm structure:

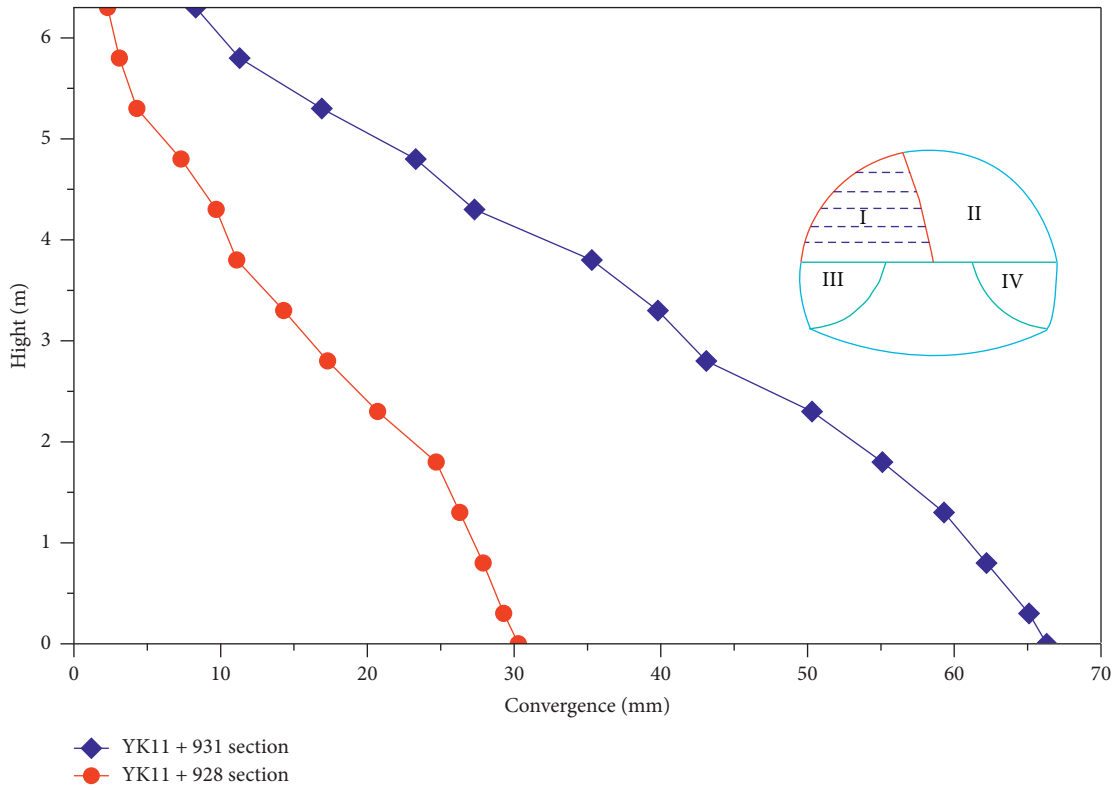

Figure 17: Horizontal convergence value in Part I.

Table 5: Relative errors for horizontal convergence value in Part I.

Section pile number	Location of measuring points	Model calculation value (mm)	Field monitoring value (mm)	Relative error (%)
YK11 + 931	Arch waist	39.8	35.0	13.7
	Maximum excavation line position	67.1	57.0	17.8
YK11 + 928	Arch waist	15.3	12.0	27.5
	Maximum excavation line position	29.3	26.0	12.7

$$\omega = \omega_l \sin \alpha + \omega_H. \quad (29)$$

According to the field measured engineering data and the above formulas, the horizontal convergence of Part I at sections YK11 + 928 and YK11 + 931 can be calculated as shown in Figure 17.

According to Figure 17, the horizontal convergence in Part I increases from top to bottom of tunnel, which is consistent with the monitoring data and field situation in tunnel project. After the excavation of Part I, the steel rib of sidewall and central diaphragm are squeezed to the interior under the rock mass pressure, so the horizontal convergence gradually increases. The maximum horizontal convergence values of YK11 + 931 and YK11 + 928 sections are 66.3 mm and 30.8 mm, respectively, and the maximum values appear at the maximum excavation line position. Relative errors for horizontal convergence value in Part I are illustrated in Table 5.

6. Conclusions

Based on the field monitoring and measurement of Wangcun tunnel, this paper analyzes the crown settlement and horizontal convergence of primary support steel rib and the central diaphragm steel rib during the construction by upper bench CD method. At the same time, the mechanical calculation model for sidewall steel rib and the central diaphragm steel rib bearing the load and deformation together is established, and the deformation for the supporting structure in tunnel project is calculated by the mechanical model. The main conclusions are as follows:

(1) With the excavation of each part in tunnel, the settlement value of monitoring point on the sidewall and the central diaphragm changed obviously, which shows the characteristics of increasing first and then gradually stabilizing. The accumulated settlement of sidewall steel rib in Part I is greater than that of the

sidewall steel rib in Part II, and the accumulated settlement of each part at the support structure during the tunnel excavation is less than the reserved deformation of 150 mm specified in the tunnel excavation. The settlement at the waist and maximum excavation line position of central diaphragm at the research section after the excavation of Parts I and II accounts for about 90% of the total settlement before the removal of central diaphragm structure, which shows that the settlement at the waist and maximum excavation line position of central diaphragm are mainly affected by the excavation of Parts I and II. During the whole excavation process, it can be seen that the excavation of Part I and Part II in tunnel has the greatest influence on the convergence at the arch waist and the maximum excavation line position, and the convergence at above two positions has experienced four stages of "convergence-expansion-convergence-gradual stability."

(2) The steel rib of sidewall and central diaphragm bear loads and deformation together under the rock mass pressure in the construction used upper bench CD method and the internal force transfer, deformation coordination, and arch foot displacement between the two structures should be considered. The sidewall steel rib is regarded as the arch structure and the equal diameter arc, the center diaphragm is regarded as the beam structure and is erected along the arc radius direction, and the support system is regarded as the arch-beam fixed structure with three times of statically indeterminate and movable abutment under the loads.

(3) With structural mechanics, the mechanical model of the steel rib of sidewall and central diaphragm is established. The model is applied to analyze and calculate the horizontal convergence at the arch waist and maximum excavation line position in Part I and the deformation of central diaphragm with the disappearance of loads in Part II, and the results are compared with the field monitoring data. The error between them is between 12.7% and 27.5%, and the calculation results are in good agreement with the field situation, which verifies the engineering applicability of mechanical model and calculation method in this paper.

Data Availability

The data used to support the findings of this study are included within the article.

Conflicts of Interest

The authors declare no conflicts of interest.

Acknowledgments

The authors would like to acknowledge the financial support provided by the National Key R&D Program of China (Grant no. 2018YFB1600100), the National Natural Science Fund Project of China (Grant nos. 51978065 and 51678063), the China Postdoctoral Science Foundation (Grant no. 2016M602738), the Chang Jiang Scholars Program (Grant no. Q2018209), and the Graduate Research Innovation Practice Project of Chang'an University (Grant no. 300103703023).

References

[1] Y. Luo, J. Chen, Y. Chen, P. Diao, and X. Qiao, "Longitudinal deformation profile of a tunnel in weak rock mass by using the back analysis method," *Tunnelling and Underground Space Technology*, vol. 71, pp. 478–493, 2018.

[2] Y. Luo, J. Chen, W. Xi et al., "Analysis of tunnel displacement accuracy with total station," *Measurement*, vol. 83, pp. 29–37, 2016.

[3] Y. Luo, J. Chen, W. Xi et al., "Application of a total station with RDM to monitor tunnel displacement," *ASCE Journal of Performance of Constructed Facilities*, vol. 31, no. 4, Article ID 04017030, 2017.

[4] J. Chen, Q. Wang, J. Guo et al., "Mechanical properties and acoustic emission characteristics of karst limestone under uniaxial compression," *Advances in Materials Science and Engineering*, vol. 2018, Article ID 2404256, 14 pages, 2018.

[5] J. Chen, W. Liu, L. Chen et al., "Failure mechanisms and modes of tunnels in monoclinic and soft-hard interbedded rocks: a case study," *KSCE Journal of Civil Engineering*, vol. 24, no. 4, pp. 1357–1373, 2020.

[6] W. Liu, J. Chen, L. Chen, Y. Luo, Z. Shi, and Y. Wu, "Nonlinear deformation behaviors and a new approach for the classification and prediction of large deformation in tunnel construction stage: a case study," *European Journal of Environmental and Civil Engineering*, pp. 1–29, 2020.

[7] Y. Zhao, H. He, and P. Li, "Key techniques for the construction of high-speed railway large-section loess tunnels," *Engineering*, vol. 4, no. 2, pp. 254–259, 2018.

[8] Y. Luo, J. Chen, W. Liu et al., "The energy-saving of urban tunnel ventilation based on the investigation of the annual discount rate of CO baseline emission in city of Shenzhen," *Journal of Testing and Evaluation*, vol. 47, no. 4, pp. 3041–3058, 2019.

[9] J. Chen, M. Wang, J. Xuan, and X. Qiao, "Deformation rule of loess highway tunnel with two lanes," *Journal of Traffic and Transportation Engineering*, vol. 12, no. 3, pp. 9–18, 2012.

[10] X. Xue, Y. Xie, and X. Zhou, "Study on the life-cycle health monitoring technology of water-rich loess tunnel," *Advances in Materials Science and Engineering*, vol. 2019, Article ID 9461890, 12 pages, 2019.

[11] X. Xue, J. Zhang, and X. Zhou, "Reliability evaluation of water-rich loess tunnel with lining crack based on extension theory," *Advances in Civil Engineering*, vol. 2019, Article ID 8267406, 10 pages, 2019.

[12] Z. Hu, K. Du, J. Lai, and Y. Xie, "Statistical analysis of influence of cover depth on loess tunnel deformation in NW China," *Advances in Civil Engineering*, vol. 2019, Article ID 2706976, 12 pages, 2019.

[13] J. Li, S. Shao, and S. Shao, "Collapsible characteristics of loess tunnel site and their effects on tunnel structure," *Tunnelling and Underground Space Technology*, vol. 83, pp. 509–519, 2019.

[14] Y. Li, S. Xu, H. Liu, E. Ma, and L. Wang, "Displacement and stress characteristics of tunnel foundation in collapsible loess

ground reinforced by jet grouting columns," *Advances in Civil Engineering*, vol. 2018, Article ID 2352174, 16 pages, 2018.

[15] X. H. Xue and Z. M. Su, "Analysis of the mechanical property of collapse in shallow-buried loess tunnel under unsymmetrical pressure," *Advanced Materials Research*, vol. 645, pp. 426–429, 2013.

[16] J. Chen, Y. Luo, and L. Chen, "Rewriting the history of loess tunnel construction," *China Highway*, vol. 11, pp. 30–35, 2019.

[17] P. Li, Y. Zhao, and X. Zhou, "Displacement characteristics of high-speed railway tunnel construction in loess ground by using multi-step excavation method," *Tunnelling and Underground Space Technology*, vol. 51, pp. 41–55, 2016.

[18] Y. Luo, J. Chen, S. Gao, X. Deng, and P. Diao, "Stability analysis of super-large-section tunnel in loess ground considering water infiltration caused by irrigation," *Environmental Earth Sciences*, vol. 76, no. 22, p. 763, 2017.

[19] S. Song, S. Li, L. Li et al., "Model test study on vibration blasting of large cross-section tunnel with small clearance in horizontal stratified surrounding rock," *Tunnelling and Underground Space Technology*, vol. 92, Article ID 103013, 2019.

[20] A. Jiang, P. Li, and H. Shi, "Shallow depth of the tunnel excavation response research based on CRD method," *Procedia Engineering*, vol. 15, pp. 4852–4856, 2011.

[21] G. Ma, H. Zheng, and P. Li, "Displacement characteristics for a "π" shaped double cross-duct excavated by cross diaphragm (CRD) method," *Tunnelling and Underground Space Technology*, vol. 77, pp. 204–215, 2018.

[22] Z. Wang, W. Yao, Y. Cai, B. Xu, Y. Fu, and G. Wei, "Analysis of ground surface settlement induced by the construction of a large-diameter shallow-buried twin-tunnel in soft ground," *Tunnelling and Underground Space Technology*, vol. 83, pp. 520–532, 2019.

[23] C. Cai, C. Shi, M. Lei, L. Peng, and R. Bai, "Deformation characteristics and countermeasures of shallow and large-span tunnel under-crossing the existing highway in soft soil: a case study," *KSCE Journal of Civil Engineering*, vol. 22, no. 8, pp. 3170–3181, 2018.

[24] M. Sharifzadeh, F. Kolivand, M. Ghorbani, and S. Yasrobi, "Design of sequential excavation method for large span urban tunnels in soft ground—niayesh tunnel," *Tunnelling and Underground Space Technology*, vol. 35, pp. 178–188, 2013.

[25] Z. Zhang, Z. Feng, and J. Li, "Application and popularization of half bench CD construction method in large-span mountain tunnel," *Highway*, vol. 62, no. 9, pp. 1–3, 2017, in Chinese.

[26] Y. Liu and H. Lai, "Load characteristics of tunnel lining in flooded loess strata considering loess structure," *Advances in Civil Engineering*, vol. 2019, Article ID 3731965, 13 pages, 2019.

[27] J. Lai, J. Qiu, H. Fan et al., "Corrigendum to "fiber bragg grating sensors-based in situ monitoring and safety assessment of loess tunnel," *Journal of Sensors*, vol. 2019, Article ID 2972178, 1 pages, 2019.

[28] S. Hu, D. Zhang, and M. Wang, "The mechanical response of the surrounding rock caused by the excavation of loess tunnel with large cross section," *China Railway Science*, vol. 32, no. 5, pp. 50–55, 2011, in Chinese.

[29] J. Zhang, M. Wang, and S. Yu, "Safety analysis of central diaphragm in CRD construction section of Xiamen east passage," *Highway*, vol. 2008, no. 3, pp. 207–211, 2008, in Chinese.

[30] J. Zhang, "Construction safety analysis of large section shallow buried tunnel by CRD method," *Railway Construction*, vol. 2008, no. 8, pp. 67–70, 2008, in Chinese.

[31] Y. Luo and J. Chen, "Deformation monitoring and analysis of diaphragm in CRD construction of shallow soil tunnel," *Modern Tunnel Technology*, vol. 48, no. 6, pp. 105–109, 2011, in Chinese.

[32] J. Zhang, X. Cao, T. Chen et al., "Calculation method of surrounding rock pressure of shallow tunnel," *Journal of Underground Space and Engineering*, vol. 13, no. 1, pp. 28–33, 2017, in Chinese.

[33] Y. Luo, J. CHEN, P. Huang, M. Tang, X. Qiao, and Q. Liu, "Deformation and mechanical model of temporary support sidewall in tunnel cutting partial section," *Tunnelling and Underground Space Technology*, vol. 61, pp. 40–49, 2017.

[34] China Communications Press, *Specifications for Design of Highway Tunnels: (JTG 3370. 1-2018)*, China Communications Press, Beijing, China, 2018, in Chinese.

[35] L. Chen, Y. Zhang, Z. Ma et al., "Analysis of combined bearing capacity of anchor bolt and steel arch in soft rock tunnel," *Journal of Rock Mechanics and Engineering*, vol. 34, no. 1, pp. 129–138, 2015, in Chinese.

[36] L. Chen, Y. Zhang, and Z. Ma, "Theoretical study on the reasonable angle of anchor pipe," *Journal of Rock Mechanics and Engineering*, vol. 34, no. 7, pp. 1334–1344, 2015, in Chinese.

[37] Y. Luo and J. Chen, "Mechanical characteristics and mechanical calculation model of anchor bolt in soft surrounding rock tunnel," *Journal of Geotechnical Engineering*, vol. 35, no. 8, pp. 1519–1525, 2013, in Chinese.

[38] Y. Long, *Calculation of Beams on Elastic Foundation*, pp. 14–26, People's Education Press, Beijing, China, 1982, in Chinese.